Light Up CRISPR: Imaging-guided Gene-editing for Comprehensive Cancer Theranostics

Yuanwei Wang,[a,b]‡ Penghang Chen,[c,d]‡ Haifei Wen,[e] Yixiong Gui,[b] Dingyuan Yan,[b] Di Huang,[d] Dong Wang,[b] Ben Zhong Tang,[e]* and Hui Tan[a]**

[a] Center for Child Care and Mental Health (CCCMH), Shenzhen Children's Hospital, Shenzhen 518034, China

[b] Center for AIE Research, Shenzhen Key Laboratory of Polymer Science and Technology, Guangdong Research Center for Interfacial Engineering of Functional Materials, College of Materials Science and Engineering, Shenzhen University, Shenzhen 518060, China

[c] Institute of Lung Health and Immunity (LHI) and Comprehensive, Pneumology Center (CPC), Helmholtz Munich, Member of the German Center for Lung Research (DZL), 85764 Neuherberg, Germany

[d] Light Innovation Technology Ltd., Shenzhen 518110, China

[e] School of Science and Engineering, The Chinese University of Hong Kong, Shenzhen (CUHK-Shenzhen), Guangdong, 518172, P.R. China

*Corresponding authors. E-mail: wangd@szu.edu.cn; tangbenz@cuhk.edu.cn; huitan@email.szu.edu.cn

‡Equally contributed to this work.

ABSTRACT. Immunotherapy combined with phototherapy is emerging as a promising strategy to treat omnipotent cancers. In this study, a clustered regularly interspaced short palindromic repeats (CRISPR)-associated protein 9 (Cas9) system, aggregation-induced emission (AIE) photosensitizer (PS) and surface coating of polyethylene imine/hyaluronic acid were combined to construct a multifunctional nanoplatform, denoted as TCPH nanoparticles (NPs), for comprehensive cancer theranostics. TCPH NPs are featured by intrinsic functions including efficient reactive oxygen species (ROS) production, good photothermal conversion, programmed death-ligand 1 (PD-L1)-eliminating capability, and effective intracellular transport. The generated ROS and hyperthermia do not only achieve primary tumor elimination but also regulate the tumor immune microenvironment. Genomic disruption of PD-L1 conspicuously augments its therapeutic efficacy, especially in tumor metastasis and recurrence. Exceptional multimodal imaging navigation has also been developed. Excellent theranostics performance was substantiated in diverse tumor models, implying that this synergistic strategy of phototheranostics and immunotherapy provides a paradigm shift in emerging CRISPR-mediated nanomedicines.

KEYWORDS. immunotherapy, phototherapy, cancer theranostics, CRISPR, aggregation-induced emission

The past decades have witnessed prosperous advancements in immunotherapy consolidating its importance in cancer therapy, among which, the immune checkpoint blockade (ICB) is of substantial clinical superiority with a subset of patients experiencing durable tumor regression.[1-3] Programmed death-ligand 1 (PD-L1), which is commonly upregulated on the surface of tumor cells, inhibits antitumor T-cell immunity processes including cytolytic activity, proliferation, and cytokine release, by binding to programmed death 1 (PD-1) expressed on lymphocytes.[4-6] Blocking PD-1/PD-L1 has been highlighted as one of the most important strategies for suppressing antitumor immunity, and monoclonal antibodies directed at PD-L1 have been approved by the US Food and Drug Administration.[7-11]

Considering that PD-L1 monoclonal antibodies are facing the drawbacks of immune-related adverse events, new technologies are urgently needed. Recently, the clustered regularly interspaced short palindromic repeats (CRISPR)-associated protein 9 (Cas9) system, composed of a Cas9 nuclease and a single guide RNA (sgRNA), has emerged as an unprecedented technology for treating various diseases through transformational genome editing of target tumorigenic or antitumorigenic genes.[12-19] The direct suppression of PD-L1 expression in tumor cells through CRISPR-Cas9 genome editing enjoys superiorities in terms of specificity and efficiency, and is considered highly promising for cancer immunotherapy.[20]

Despite this remarkable progress, ICB response rates vary across tumor types, and CRISPR suffers from low targeting efficiency, leading to unsatisfactory therapeutic efficiency in clinical trials.[21-22] Thus, it is imperative to formulate multifunctional materials that hold merits of multifarious therapeutic models to improve cancer treatment outcomes.[23-24]

As a promising protocol employing light to generate localized reactive oxygen species (ROS) for conducting photodynamic therapy (PDT) and hyperthermia for implementing photothermal therapy (PTT), phototherapy has been eagerly pursued in the field of tumor therapy by virtue of its noninvasive and spatiotemporally controllable features.[25-26] Apart from directly killing malignant cells through ROS or hyperthermia, phototherapy also emerges as a favorable modality to induce immunogenic cell death (ICD), which can reshape the tumor microenvironment by releasing tumor-associated antigens as immunostimulatory "danger" signals.[27-31] Furthermore, the activation of tumors by phototherapy negatively upregulates the expression level of PD-L1, which accounts for the immune regulation mechanism in tumor cells. Accordingly, the ingenious construction of versatile system allowing simultaneous CRISPR-Cas9 genome-mediated immunotherapy and synergistic phototherapy would be vitally important.

Given the circumstances, photosensitizers with aggregation-induced emission (AIEgens) features are admirable candidates to implement synergistic phototherapy even multimodal

phototheranostic, due to their prominent performance in both phototherapy and imaging navigation, including fluorescence imaging (FLI), photoacoustic imaging (PAI) and photothermal imaging (PTI), providing high diagnostic sensitivity and temporal resolution.[32-33] To facilitate the practical applications of AIEgens, various proteins, including bovine serum albumin (BSA) and fetal bovine serum (FBS), have been widely used in loading and delivering AIEgens.[34-35] The unique fold structure of proteins endows AIEgens with ideal accommodation through a mechanism of restriction of intramolecular motions (RIM), and improves surface properties of AIEgens through system engineering, encompassing stability, compatibility, and functionality in physiological environments.[32,36-37] Consequently, it is highly necessary to fabricate preeminent AIEgens-based protein nanoplatforms for comprehensive cancer phototheranostics outcomes.

In this study, we developed a multifunctional nanoplatform for potent cancer theranostics, denoted as TCPH, through a layer-by-layer electrostatic adsorption process (Scheme 1A). First, a typical AIEgen, namely TTT, was encapsulated in the pleated interspaces of the Cas9 protein, which amplified fluorescence emission. Together with the sgRNA plasmid, designed to target PD-L1, the composites were enveloped by the cationic polymer, polyethylene imine (PEI), which enabled lysosomal escape and facilitated nuclear transport afterward by the nuclear localization sequence (NLS) of the Cas9 protein.[38-39] Hyaluronic acid (HA), an

anionic polymer with good biocompatibility, can provide a negatively charged surface for blood circulation and target cell surface differentiation cluster 44 (CD44) receptors, which are highly expressed in various tumor cells, to enhance tumor targeting efficiency.[40-41] The downregulation of PD-L1 expression by CRISPR-Cas9 technology restores the antitumor activity of T cells and suppresses tumor cell growth. In contrast, TTT molecules play pivotal roles in phototheranostics, providing sufficient ROS/heat and excellent imaging performance upon NIR laser irradiation. Meanwhile, a slight temperature increase is commendable in impeding the tumor thermo-resistance effect, turning cold tumors to hot tumors, improving immunotherapy outcomes.[42-44] Particularly, it has been shown that the second near-infrared (NIR-II, 1000-1350 nm) optical window fluorescence of TTT offers additional advantages such as reduced photon scattering, low tissue background, and deeper tissue penetration.[45-46] Consequently, multimodal imaging (FLI/PAI/PTI) guided synergistic phototherapy-immunotherapy has been realized for potent cancer phototheranostics in various models, which poses immense potential for clinical applications (Scheme 1B).

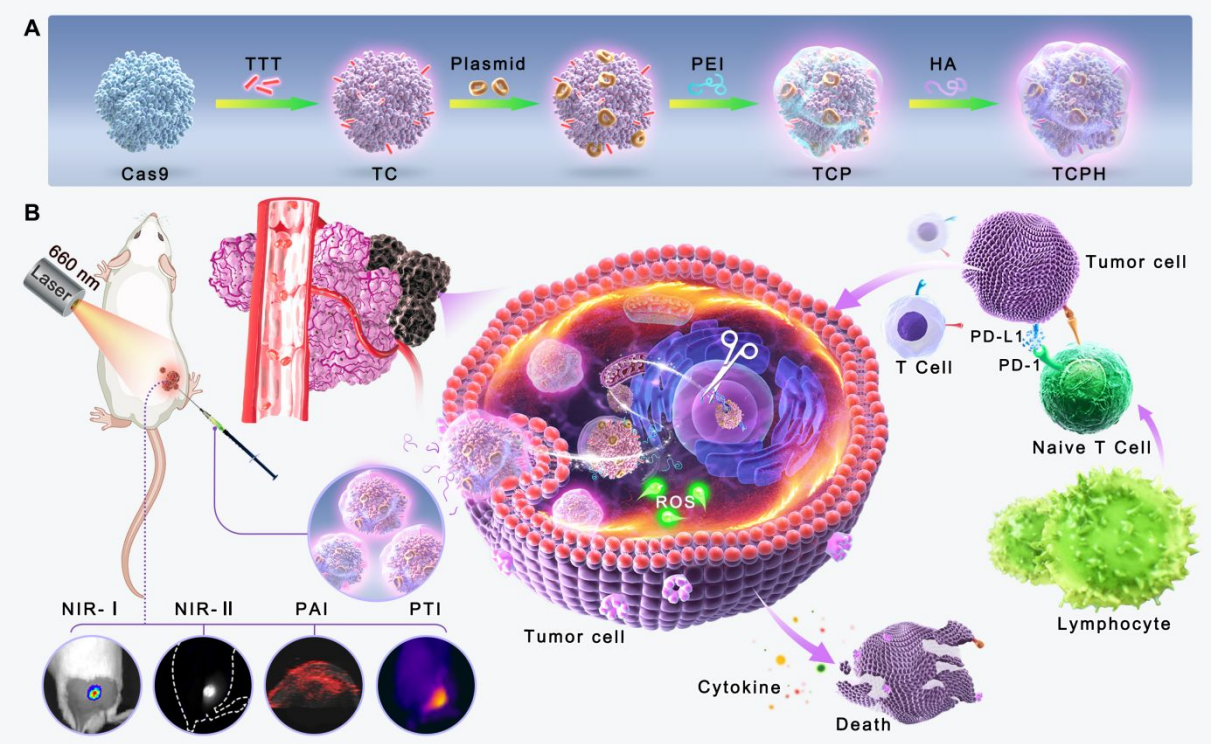

Scheme 1. Schematic illustration of nanofabrication and versatile theranostic application. (A) Construction of TCPH NPs using an assembly strategy. (B) Illustration of the application of TCPH NPs on NIR-I/II FLI/PAI/PTI trimodal imaging-guided PDT/PTT/immunotherapy in synergistic cancer theranostics.

RESULTS AND DISCUSSION

Construction, characterization, and structural-activity investigation. TTT are structurally featured by extended π-conjugation length, strong electron donor-acceptor-donor (D-A-D) effect and twisted conformation.[47] The AIE tendency of TTT was determined by comparing its photoluminescence (PL) intensity in toluene and dimethyl sulfoxide (DMSO) mixtures with different toluene fractions (Figure S1), where the PL intensity gradually increased along

with the addition of toluene (Figure 1A). The maximum absorption peak of TTT in DMSO was at 544 nm, and its maximum emission peaked at 789 nm (Figure 1B, dashed line). Due to the addition of proteins and their confinement effect, the absorption band of TCPH increased remarkably in the UV region, and a dramatic bathochromic shift of approximately 114 nm was observed in the emission spectrum (Figure 1B, solid line), which extended to the NIR-II region.

According to the unique characteristics of AIEgens, the aggravated confinement environment resulting from the protein constraints is considered responsible for the changes in optical properties. To verify this conjecture, Cas9 (0-8 μg/mL) was introduced into TTT aqueous solution (1 μg/mL) in increasing quantities. Along with the addition of Cas9, the PL intensity of the composites gradually increased, accompanied by a discernible bathochromic shift of 32 nm, which implied a conformational change in TTT (Figure 1C). Furthermore, increasing amounts of TTT were introduced into a fixed Cas9 aqueous medium, where the weight ratios of TTT and Cas9 were 0.01:1, 0.05:1, 0.1:1, 0.5:1, and 1:1. As evident from the PL spectra and the corresponding maximum intensity ratios (Figure 1D and Figure S2), the amplification effect reached a peak when the weight ratio of TTT to Cas9 was ultimately 0.1:1, which was determined to be the optimal feeding ratio.

Molecular docking calculations were performed to validate the interaction between TTT and Cas9 (Figure 1E). The benzothiazole segment was buried in a groove surrounded by HIS-328, ILE-363, and TYR-325 through a π-π stacking with HIS-328. The triphenylamine moiety is occupied the well-tailored pocket formed by the residues HIS-160, ALA-157, and LEU-153 through a T-shaped π-π interaction with HIS-160. Detailed calculations demonstrated that the major interactions between TTT and Cas9 were hydrophobic (Figure S3 and Table S1), and the lowest binding energy was -8.47 kcal/ mol, indicating a promising construction strategy for hydrophobic PSs.

Transmission electron microscopy (TEM) and dynamic light scattering (DLS) were used to examine the morphology of the developed TCPH nanoparticles (NPs), which were deciphered as uniform nanospheres with a mean diameter of approximately 191 nm (Figure 1F and Figure 1G). The existence of TTT in TCPH NPs was evidenced by energy dispersive spectrometer element analysis, where the weight ratio of S was 4.02%, whereas those of O and C were 56.6% and 39.38%, respectively (Figure 1F). Furthermore, a recurrent reversal of the surface potential was observed, accompanied by a lay-by-lay absorption process for each component, which eventually resulted in a slightly negative surface, which was beneficial for blood circulation (Figure 1H). Because of their physiologically stable structure, TCPH NPs exhibited considerably superior stability compared to bare TTT NPs. When stored in

phosphate-buffered saline (PBS) at 4 ˚C, imperceptible changes in the size of TCPH NPs were observed at 168 h, whereas obvious precipitation of TTT NPs was observed within 24 h, which resulted in undetectable size distribution (Figure 1I). Physiological stability is essential for subsequent in vivo studies.

TCPH NPs possessed excellent capabilities for ROS generation and photothermal conversion, which inherited from TTT molecules. ROS generation was assessed using dichlorodihydrofluorescein diacetate (DCFH-DA) as an indicator, the fluorescence of which can be triggered by ROS. A remarkable increase in PL intensity was observed in the TCPH sample compared to the commercial PS chlorin e6 sample (Ce6) (Figure 1J and Figure S4). Furthermore, the photothermal conversion performance of TCPH was evaluated, which demonstrated excellent photothermal conversion capability and long-term stability (Figure 1K and Figure S5). Overall, excellent antitumor performance can be guaranteed in potent phototherapy.

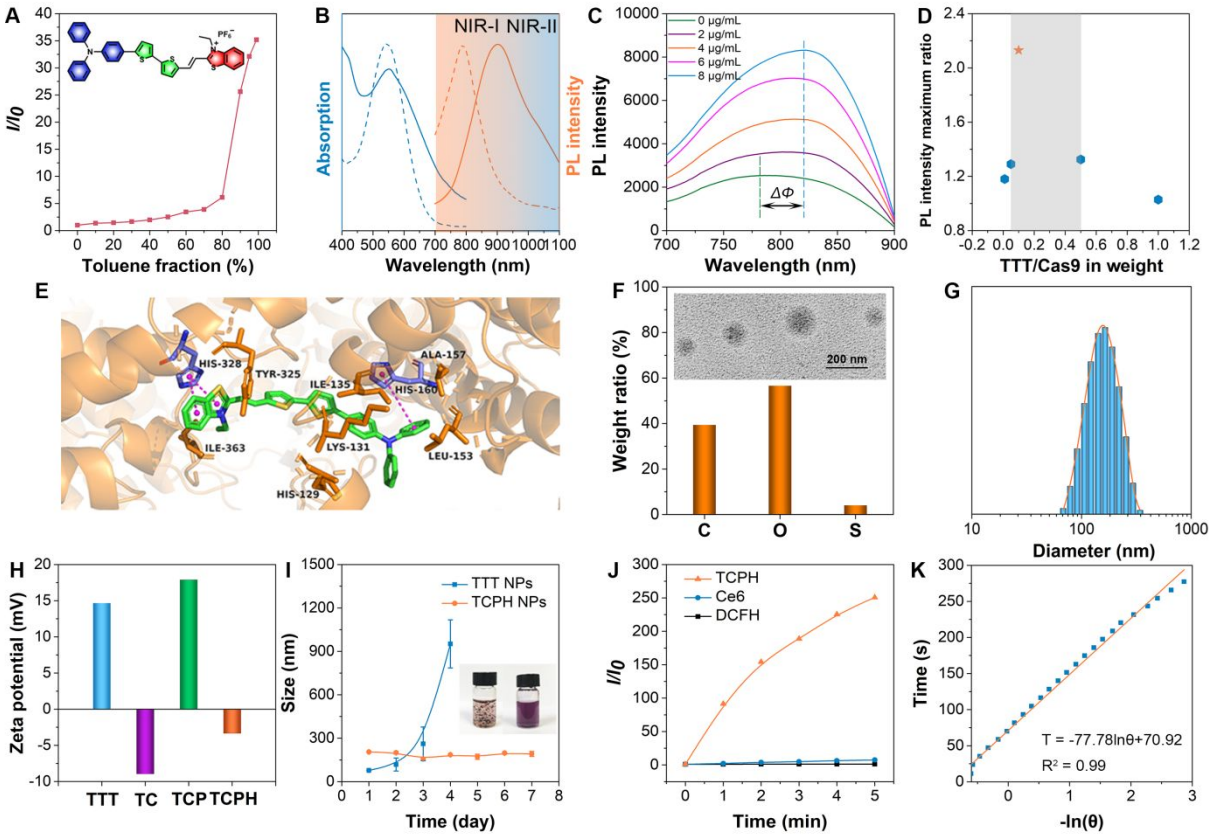

Figure 1. Construction and characterization of TCPH. (A) Plots of the relative emission intensity (I/I_0) versus the toluene fraction. I_0 and I are the peak values of the PL intensities of TTT in DMSO and DMSO/toluene mixtures, respectively. (B) Normalized absorption and PL spectra of TTT in the DMSO solution (dash line) and TCPH in water (solid line). (C) The PL spectra when increasing concentrations of Cas9 were introduced into 1 μg/mL TTT aqueous solution. (D) The maximum ratio of PL intensity between TTT and TC when TTT and Cas9 were present in weight ratios of 0.01:1, 0.05:1, 0.1:1, 0.5:1, and 1:1, respectively. (E) The molecular docking model of TTT and Cas9. (F) The weight ratio of O, C, and S in TCPH NPs and their TEM image insert. (G) The size distribution of TCPH NPs in an aqueous medium. (H) The zeta potential of TTT, TC, TCP, and TCPH in aqueous medium. (I)The particle size

tracking of TTT NPs and TCPH NPs stored in PBS at 4 ˚C for seven days. (J) ROS generation by TCPH upon 660 nm laser irradiation (0.3 W/cm^2) in contrast with Ce6, indicated by DCFH-DA. (K) Linear time data versus -ln θ obtained from the cooling period versus negative natural logarithm of the driving force temperature for TCPH.

Intracellular function route and antitumor performance investigation. Before *in vivo* therapeutic investigation, it is necessary to confirm the effectiveness of the designed TCPH NPs against cancer cells. The light-induced tumoricidal effects of TCPH on 4T1 cells were investigated using a CCK-8 assay (Figure 2A). TCPH NPs were faintly toxic to 4T1 tumor cells in the dark at the tested concentration range of 0-100 μg/mL, indicating their extraordinary biosafety intuitively. At 660 nm laser irradiation, the profiles of cell viability *versus* TTT concentration exhibited an IC_{50} value (the concentration causing 50% growth inhibition) of 6.8 μg/mL, manifesting the phototherapy-triggered tumoricidal effects. Western blot (WB) analysis demonstrated that PD-L1 expression was apparently suppressed in 4T1 cells treated with TCPH NPs after genome editing for 48 h (Figure 2B), indicating that the introduction of TTT and light irradiation had an indiscernible influence on the gene-editing performance of the CRISPR-Cas9 system.

Their intracellular performances were investigated. Intracellular ROS generation was indicated by DCFH (Figure 2C, upper row). The introduction of laser irradiation on both TTT and TCPH-treated 4T1 cells resulted in bright green fluorescence, whereas the absence of laser irradiation resulted in non-fluorescence, disclosing the feasibility and controllability of ROS generation under NIR-mediation. Furthermore, calcein and propidium iodide (CA/PI) double staining was applied to distinguish between live (green) and dead (red) 4T1 cells (Figure 2C, middle row). As predicted, numerous dead 4T1 cells were observed in the TTT + L group and the TCPH + L group, indicating their excellent photoablation capabilities against cancer cells.

Subsequently, the extent of DNA damage in treated 4T1 cells was assessed using the comet assay, where the degree of DNA damage was signified by the tail length of fluorescence-stained DNA. As preconceived, the most pronounced comet tails were observed in the TCPH + L group, whereas the TTT + L group exhibited moderate comet tails (Figure 2C, lower row). In detail, 51.25% DNA damage was observed in the 4T1 cells in the TCPH + L group, which starkly contrasted with that in the TTT + L group (29.07%) and other control groups (5.46%, 11.92%, and 11.30% in the PBS group, TTT group, and TCPH group, respectively), as substantiated by the statistical results of the tail DNA percentage (Figure S6). The olive moment and tail moment analyses results demonstrated that phototherapy-induced DNA

damage was further exacerbated with the assistance of the CRISPR delivery system, which was further exacerbated in the following context.

To evaluate the intracellular delivery route of TCPH NPs, a colocalization analysis of TCPH and TTT NPs with various subcellular organelles in 4T1 cells was performed. The nuclear, lysosomes, and mitochondria were stained with 4',6-diamidino-2-phenylindole (DAPI), Lyso Tracker Green, and MitoTracker Green, respectively (Figure 2D). In the first hour, TCPH NPs were efficiently captured by lysosomes with a Pearson colocalization coefficient of 73.13%, whereas some TTT NPs still enrich on the cell membrane. Benefiting from the proton sponge effect of PEI, TCPH NPs effectively escaped from the lysosomes and entered mitochondria after 3 h of incubation, with a Pearson colocalization coefficient of 83.05% (Figure 2D and Figure S7). Approximately 6 h later, due to the NLS of the Cas9 protein, red fluorescence of TCPH was observed in the nuclear region, especially in the nucleolus (Figure 2D and Figure S8). In contrast, in the absence of PEI, TTT NPs were always harbored in lipid droplets or lysosomes, rather than in the mitochondria or nuclei (Figure 2D, lower row, and Figure S9). The aforementioned intracellular delivery route of TCPH NPs is intuitively illustrated in a schematic illustration (Figure 2E). As anticipated, the designed TCPH NPs exhibited exceptional performance in endocytosis, lysosomal escape, and nuclear targeting, which were beneficial for theranostics afterward.

ICD in tumor cells was investigated by analyzing the release of several damage-associated molecular patterns (DAMPs), that can bind to pattern recognition receptors on the surface of DCs, initiating a series of cellular reactions, and ultimately activating innate and adaptive immune responses. Heat shock protein 70 (HSP 70) is a member of the HSP family, and HSP 70 was usually activated to protect cells from high temperatures. Calreticulin (CRT) is a pivotal molecular chaperone protein involved in the immune response to tumors. As demonstrated by the immunofluorescence images, the amount of HSP 70 in the nuclear and CRT in the cytoplasm distinctly increased after TCPH + L treatment (Figure 2F and Figure S10), which implied a thermal and immune response after the intervention. High mobility group box 1 (HMGB1) and adenosine-triphosphate (ATP) are highly correlated with ICD. As demonstrated by the enzyme-linked immunosorbent assay (ELISA), the intracellular secretion of HMGB1 increased and that of ATP decreased after diverse therapeutic interventions (Figure 2G and Figure 2H). As anticipated, TCPH + L-mediated synergistic phototherapy-immunotherapy can efficiently induce ICD and promote antitumor effects.

Multimodal diagnosis performance on different models. The *in vivo* multimodal diagnosis performance was executed on unilateral, bilateral, and orthotopic subcutaneous 4T1 tumor models. After intratumoral injection of TCPH NPs, their distribution in tumors was determined by real-time monitoring using NIR-I and NIR-II FLI. Strong fluorescent signals

were obtained in the initial 24 h post-injection period and gradually weakened due to organ metabolism (Figure 3A and Figure 3C). After 96 h, tumor resection was successfully performed under FLI navigation in the unilateral and bilateral subcutaneous 4T1 tumor models (Figure S11). Furthermore, mice were sacrificed and the *ex vivo* FLI of isolated tissues was captured, including the heart, liver, spleen, lung, kidney, and tumor (Figure 3B and Figure 3D). Compared to other major organs, overwhelming fluorescence was observed in the flank tumors, manifesting the excellent specificity of TCPH NPs for tumors. Lung metastasis was observed as sporadic NIR-II FLI signals in the orthotopic subcutaneous 4T1 tumor model alone, implying the potential of TCPH NPs in tracking lung metastasis.

The intensity of the photoacoustic signal at the tumor site was evaluated as well. Strong PA signals were obtained in 1 h post-injection and gradually decreased over the following 72 h (Figure 3E), which was in good accordance with the FLI results. Furthermore, *in vivo* PTI showed temperature changes on the tumor surface under laser illumination with the assistance of an infrared thermal camera (Figure 3F and Figure 3G). Accompanied by the laser irradiation, the surface temperature of the tumor showed a rapid increase to 46.2 ˚C within 5 min, which facilitated the PTT process monitoring by thermal imaging.

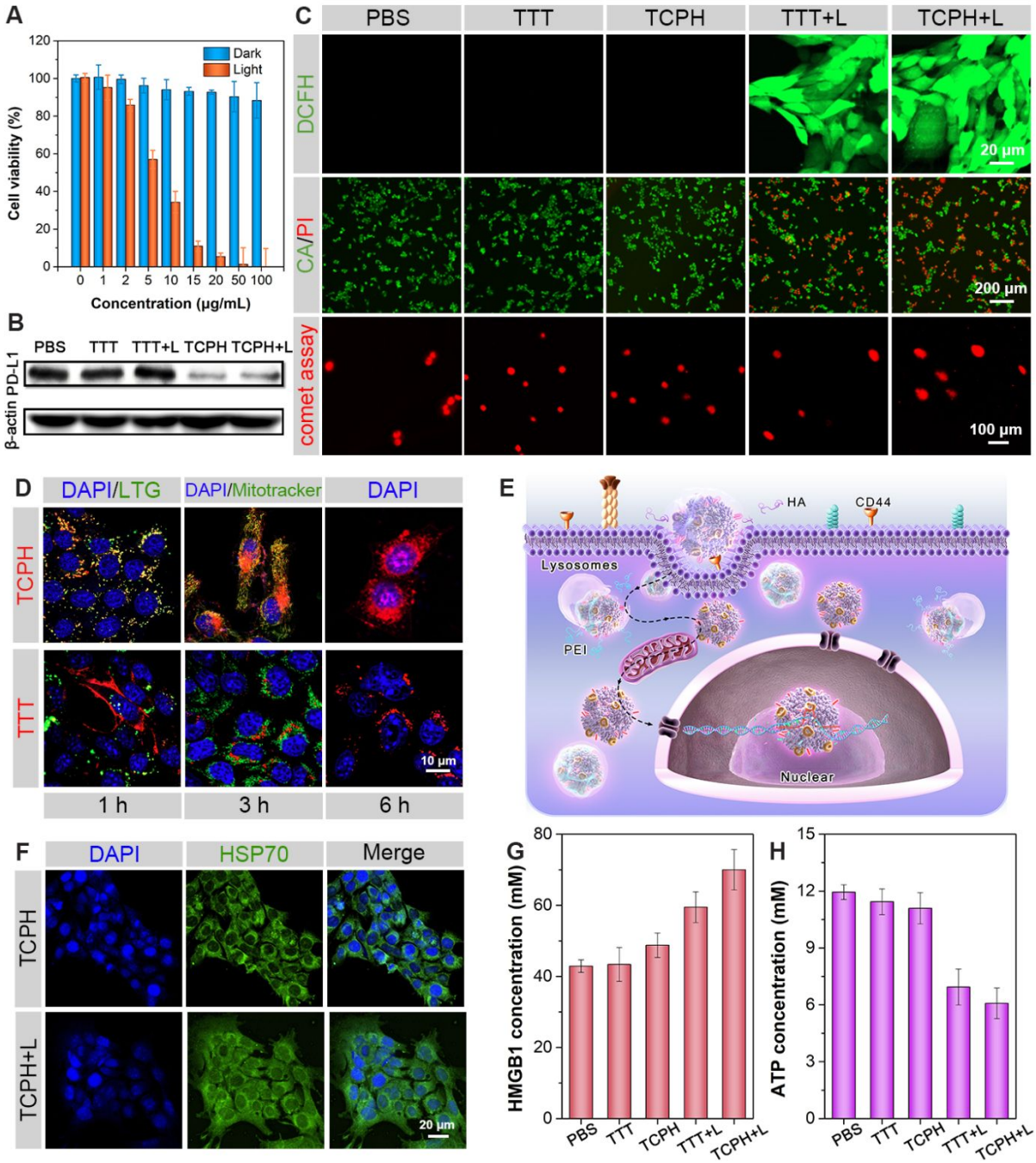

Figure 2. *In vitro* antitumor study of TCPH in 4T1 tumor cells. (A) Cell viability of 4T1 cells incubated with TCPH for 24 h at various doses with or without 660 nm laser irradiation (0.3 W/cm^2, 10 min), determined by the CCK-8 assay (mean ± standard deviation, n = 6). (B) WB patterns of 4T1 cells after different treatments. (C) Intracellular ROS generation (upper row), live/dead cell staining (middle row), and comet assay (lower row) of 4T1 cells after different

treatments. (D) CLSM images of 4T1 cells after incubation with TCPH or TTT NPs at 1, 3, and 6 h, including TTT channel (red), the lysosome channel and the mitochondrion channel (green) and nuclear channel (blue). (E) Schematic illustration of the intracellular transport process of TCPH NPs. (F) Immunofluorescence staining of 4T1 cells showing HSP70 after the different treatments. (G) Analysis of the HMGB1 and (H) ATP quantities in each group after different treatments.

***In vivo* synergistic antitumor performance on different models.** Synergistic phototherapy-immunotherapy was sophisticatedly executed in a unilateral subcutaneous 4T1 tumor model (Figure 4A). The mice were randomly divided into five groups for different treatments: (i) PBS, (ii) TTT, (iii) TCPH, (iv) TTT + L, and (v) TCPH + L. Laser irradiation (660 nm) was applied to the tumor sites at 0.3 W/cm^2 for 10 min. Changes in tumor volume were recorded during the 15-day treatment period (Figure 4B and Figure 4E). As shown in the tumor growth curve, variable degrees of tumor growth inhibition were observed, whereby TCPH + L treatment eliminated the subcutaneous tumors, whereas the TCPH and TTT + L treatments had a moderate effect on tumor inhibition. In terms of safety, the body weight of each group was recorded during treatment. Weight loss in the treatment group was within the acceptable

range during the 15-day treatment period, indicating that the drug doses were within the safe range (Figure 4C).

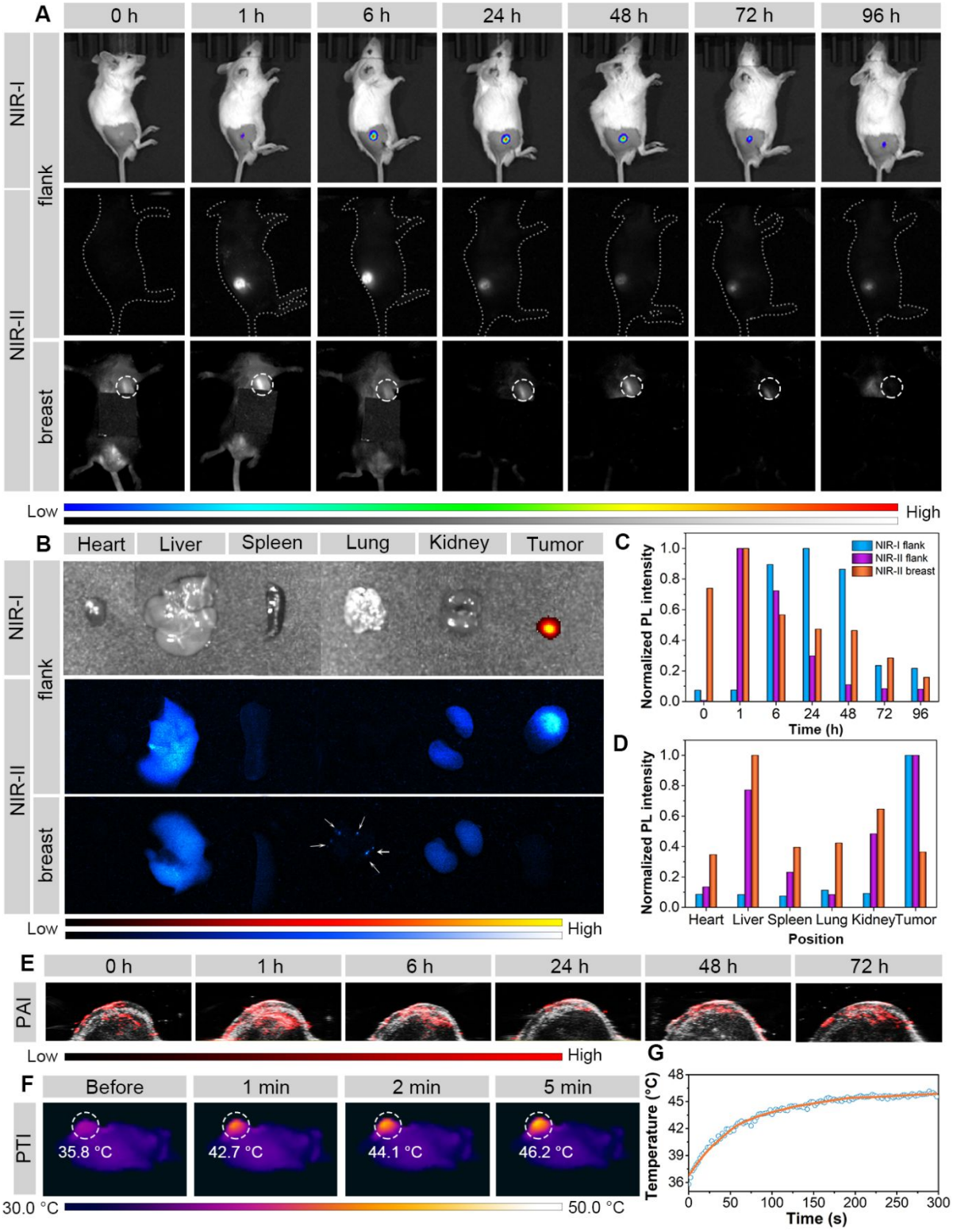

Figure 3. *In vivo* multimodal imaging of TCPH on 4T1 tumor-bearing BALB/c mice. (A) *In vivo* NIR-I and NIR-II FLI of mice after intratumoral injection of TCPH at different monitoring times and positions. (B) *Ex vivo* NIR-I FLI and NIR-II FLI of major organs and tumors harvested from the euthanized mice. (C) The corresponding normalized PL intensity of tumors and (D) major organs/tumors harvested from the euthanized mice. (E) PAI of tumor after intratumoral injection of TCPH at different monitoring times. (F) PTI and (G) the heating curves of tumor sites after 660 nm laser irradiation (0.3 W/cm^2), 24 h post-injection of TCPH.

To verify therapeutic efficacy, mice treated with the above formulations were euthanized on day 15 and subjected to histological and immunohistochemical analyses (Figure 4D). The proliferative activity of the tumors was estimated by hematoxylin and eosin (H&E) staining. Gradually increasing voids and conspicuous karyopyknosis were observed in the TTT + L and TCPH + L groups, compared with the superabundant and densely arranged tumor cells in other groups, which manifested extensive damage to tumor tissues due to synergistic phototherapy-immunotherapy. Similarly, severe apoptosis and necrosis of tumor cells in the TTT + L and TCPH + L groups were verified by a terminal deoxynucleotidyl transferase dUTP nick end labeling (TUNEL) immunofluorescence staining assay and proliferative marker expression (Ki67).

To determine the *in vivo* side effects, H&E staining was applied to the major organs (heart, liver, spleen, lung, and kidney) of the euthanized mice in the TCPH + L group after complete treatment. Apparently, neglectable tissue impairment and inflammatory lesions were observed in the TTT + L and TCPH + L groups (Figure 4D and Figure S12). As a supplement, blood biochemical analyses were also performed, where indiscernible distinction was found in both the hemolysis test (Figure 4F and Figure S13) and blood biochemistry parameters, including hepatic function markers and renal function markers (Figure 4G). These collective findings offered solid evidences for the great biosafety of TCPH NPs.

To further investigate the ICD effect, multiple cytokines in the mouse sera were examined by ELISA 3 days after TCPH + L treatment, including tumor necrosis factor α (TNF-α), interferon γ (IFN-γ) and interleukin 6 (IL-6). It was found that the secretion levels of TNF-α, IFN-γ and IL-6 were elevated after different treatments (Figure 4H). Because TNF-α is a critical mediator of cellular immunity, IFN-γ can positively regulate immune activity, and IL-6 is a typical marker of inflammation, their increased levels indicate the activation of the immunity response in the group of TCPH + L, which plays an important role in tumor immunotherapy.

To reveal the mechanisms of TCPH-mediated antitumor immunity under laser irradiation, DC maturation in tumor-draining lymph nodes (TDLNs) was evaluated. DCs in the TDLNs of

unilateral 4T1 tumor-bearing mice 7 d after treatment were collected and stained with anti-CD11c, anti-CD80, and anti-CD86 antibodies for flow cytometry analysis. Apparently, the percentage of $CD80^+$ was elevated from 10.1% to 13.3% due to PD-L1 knock out performance (Figure 4I). When combined with laser irradiation, the percentage of mature DCs increased substantially to 18.1% due to the ICD effect of phototherapy.

To further evaluate the performance of TCPH-mediated phototherapy-immunotherapy on tumor metastasis and recurrence, a bilateral subcutaneous 4T1 breast tumor-bearing mouse model was used (Figure 5A). First, a primary tumor was established on the right flank of each mouse. When the tumor volume reached ~100 mm^3, they were surgically removed, and the left flank of each mouse was inoculated with 4T1 cells on the following day. Once the secondary tumor volume reached ~100 mm^3 approximately 7 d later, the corresponding treatments were administered, and the tumor volume and body weight were monitored every other day. Based on the tumor growth curves (Figure S13a and Figure S15), PBS and TTT treatments had no distinct effect on tumor inhibition, whereas TCPH and TTT + L treatments exhibited comparable tumor-inhibition effect. In contrast, considerable tumor elimination was observed in the TCPH + L group, indicating a synergistic immune boosting and

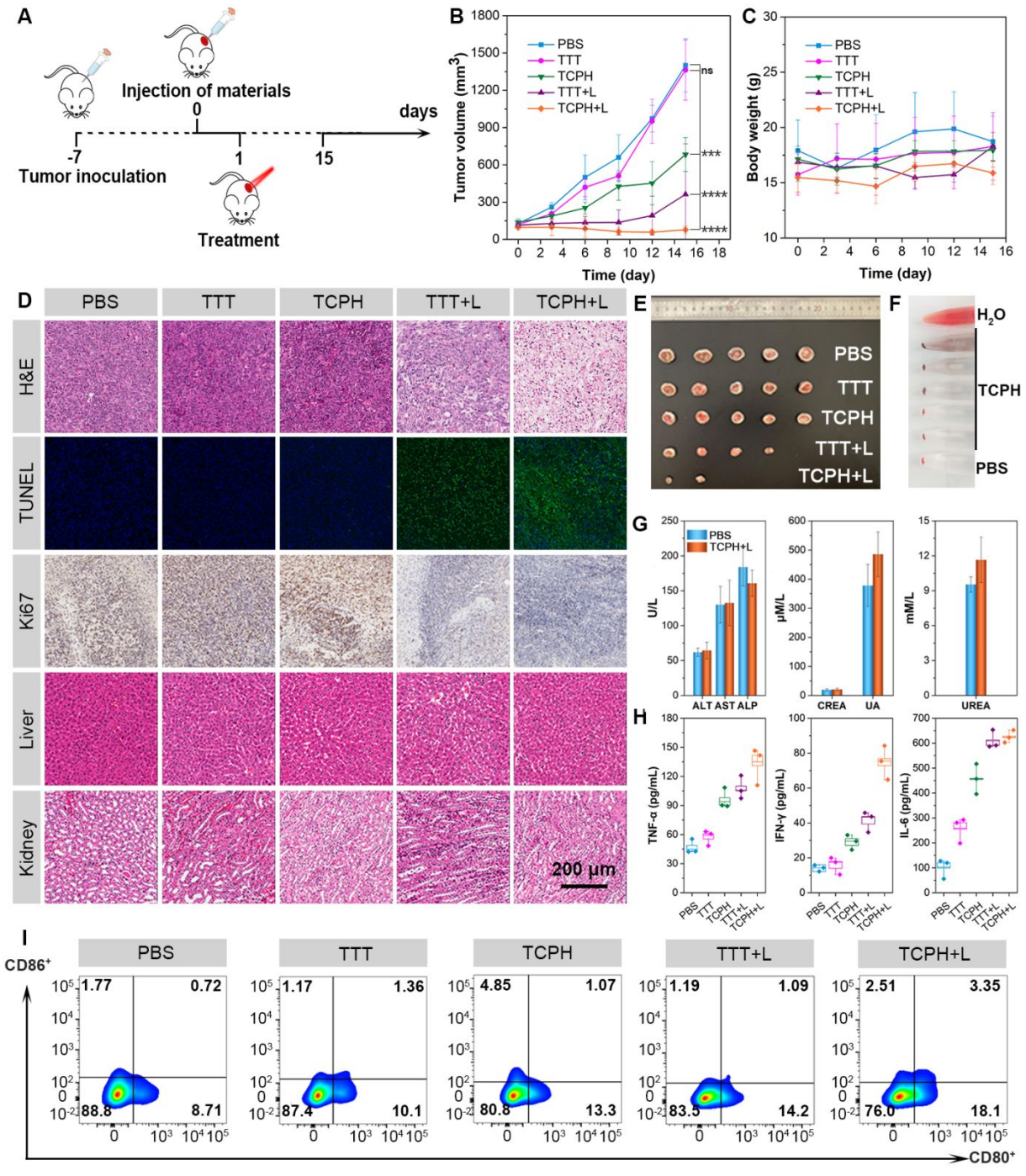

Figure 4. The antitumor efficacy of TCPH in a unilateral subcutaneous 4T1 tumor model. (A) Schematic illustration showing the in vivo PDT/PTT/immunotherapy experimental procedure. (B) Tumor volume and (C) body weight of mice after different treatments. (D) Representative H&E, TUNEL, and Ki67 staining analyses of tumor tissues and H&E staining of liver and

kidney tissues after 7 d of various treatments. TUNEL positive cells were stained in green. (E) Tumor resection and (F) hemolysis test after various treatments. (G) Hepatic function and renal function tests of mice after various treatments. (H) The cytokine levels of TNF-α, IFN-γ, and IL-6 in sera from mice isolated 3 d post-injection. (I) Representative flow cytometry plots of the percentages of mature DCs ($CD86^+/CD80^+$) in the TDLNs.

phototherapeutic effect. In the survival analysis, it was demonstrated that all mice in the TCPH + L group survived until day 60, with no evidence of tumor relapse, whereas none of the mice in the PBS group survived (Figure 5B). Body weight and photographs of the mice were recorded during the treatments (Figure S13b and Figure S16). Negligible body weight loss and a drastic elimination of both primary and distant tumors further supported the excellent tumor metastasis and recurrence inhibition efficacy of the TCPH + L treatment.

To further reveal the mechanism of the TCPH-mediated phototherapy-immunotherapy under light irradiation, we collected distant tumors 10 d after the indicated treatments, obtained a cell suspension, and analyzed cytotoxic T lymphocytes (CTLs, $CD3^+$, and $CD8^+$) expression levels through flow cytometry. The percentage of $CD8^+$ cells increased significantly from 8.35% to 13.7% and reached 28.9% after the introduction of the gene-editing process and laser irradiation (Figure 5C). Due to the synergistic effect of ICD through

phototherapy and PD-L1 knockout using CRISPR, the immunosuppressive microenvironment was significantly improved in tumor tissues, promoting CTLs recruitment.

Considering that pulmonary metastasis threatens breast cancer therapeutics, an orthotopic subcutaneous 4T1 tumor model was established in the first left first mammary gland of each mouse (Figure S17a). Therefore, the TTT and TCPH group exhibited undesirable tumor-inhibition results, whereas laser irradiation considerably improved therapeutic outcomes (Figure S17b and Figure S18). The tumors appeared to shrink after effective treatments, as shown in the photographs of the mice before and after treatment (Figure S19). Biosafety was verified by the gradual increase in body weight of each treatment group (Figure S17c). To investigate the pulmonary metastasis, pulmonary anatomy and pathological studies were performed after different treatments (Figure 5D). As depicted in the photos of the excised lungs, large amounts of metastatic nodules were present in the control group, whereas they were almost absent from the TCPH + L group. The inhibition of pulmonary metastasis was also supported by the H&E staining images of the lung, in which widely distributed tumor infiltration was observed in the control groups, whereas the TCPH + L group exhibited a healthy appearance. Light-sheet microscopy (LiSM) images of the lung also supported the pulmonary infiltration effect of the treated group, where a significantly fewer fluorescence

signals of tumors was observed in the TCPH + L group (Figure 5D lower row, indicated by the yellow circle line, and Figure S20).

In order to further validate the safety of therapy, TCPH NPs appealing to rabbits were established by adjusting the sgRNA plasmid of CRISPR-Cas9/PD-L1 system. In an orthotopic subcutaneous VX2 tumor model, which was established by implanting VX2 tumor tissue into the left first mammary gland of New Zealand white rabbits, TTT NPs and TCPH NPs were applied, respectively. As shown, both routine blood and biochemical indices were in the normal range after TCPH + L therapeutic intervention (Table S2 and Table S3). In stark contrast, slighter hepatic injury was found in the TCPH + L group, as disclosed by the hepatic function markers results (Table S3), indicating the good biosafety of TCPH NPs in therapeutic interventions.

CONCLUSION

We have successfully developed a versatile nanoplatform, namely TCPH NPs, for synergistic cancer theranostics. TCPH NPs were established by integrating an AIE-active agent TTT and CRISPR-Cas9/PD-L1 in a single formulation. Taking advantage of the unique fold structure of Cas9 proteins, the AIE features of molecules were amplified with ideal accommodation through a mechanism of RIM, resulting in exceptional imaging navigation

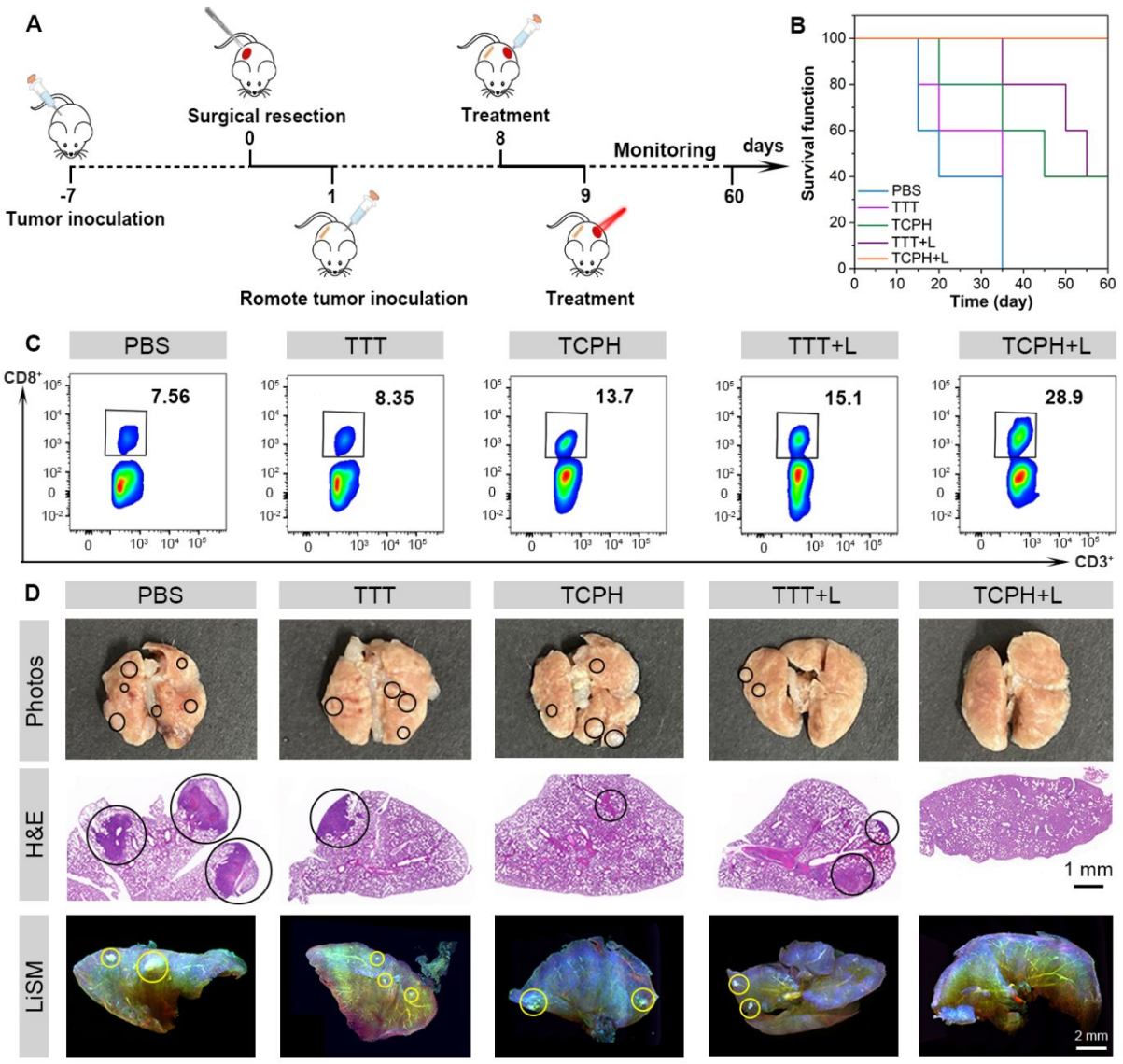

Figure 5. The antitumor efficacy of TCPH in a bilateral and orthotopic subcutaneous 4T1 tumor model. (A) Schematic illustration of the *in vivo* PDT/PTT/immunotherapy experiment procedure in a bilateral subcutaneous 4T1 tumor model. (B) The survival function of mice after different treatments. (C) Representative flow cytometry plots of the percentages of $CD3^+$ and $CD8^+$ T cells. (D) Lung resection after different treatments and the corresponding photographs, and H&E staining and LiSM images.

performance. By employing various mouse models, encompassing unilateral, bilateral, and orthotopic subcutaneous 4T1 tumor models, the presented protocol was substantiated to be effective in eliminating primary tumors and restricting lung metastasis through the synergistic intervention of phototherapy and immunotherapy. These collective findings intuitively substantiate that TCPH NPs can be used as highly versatile phototheranostic agents for FLI/PAI/PTI trimodal imaging-guided synergistic PDT/PTT/immunotherapy for cancer therapy, which holds immense potential for potent cancer theranostics.

EXPERIMENTAL SECTION

Preparation of TCPH. The TTT solution (1 μL; concentration: 1 mg/mL in DMSO) was added to the Cas9 protein solution (11.4 μL; concentration: 875 μg/mL in PBS). The mixture solution was vortexed for 10 s to obtain a transparent solution of TC NPs. Then, sgRNA plasmid solution (5 μL; concentration: 1 mg/mL in PBS) was added to the above solution. After 10 min, PEI solution (0.1 μL; concentration: 1 mg/mL in water) was added, followed by the addition of HA solution (0.1 μL; concentration: 1 mg/mL in water) to produce TCP NPs and TCPH NPs, respectively. After low-speed ultrafiltration at 4 °C, TCPH solutions with specific TTT concentrations were obtained, according to the concentration calibration curve (Figure S21). In this study, the concentration of TCPH was indicated by the TTT concentration.

Characterization of TCPH. TCPH aqueous solutions with different concentrations were continuously exposed to 660-nm laser irradiation at different intensities. The temperature was recorded every 30 s until the maximum value was obtained. TCPH aqueous solutions were exposed to repeated on-off irradiation cycles at 660 nm (0.3 W/cm^2) for 50 min. Real-time thermal images were recorded. The total ROS generation was investigated using DCFH-DA as the indicator. Generally, 3 μL of DCFH-DA solution (5 mM in PBS) was added to 3 mL of a sample solution (containing 0.1 μg/mL TCPH). The mixture was then exposed to 660-nm laser irradiation for 1 min. The indicator fluorescence was measured using a PL instrument at 525 nm upon excitation at 488 nm. TCPH and TTT were stored in PBS at 4 ˚C (containing 100 μg/mL TTT). The size distribution was monitored using DLS at fixed time points.

***In vitro* fluorescence imaging and synergistic antitumor efficacy of TCPH.** 4T1 cells were seeded at a density of 5 × 10^3 cells per well in a 96-well plate and cultured overnight, after which the existing medium was replaced with fresh medium containing different concentrations of TCPH. After 24 h of incubation and treatments, the cells were cultured overnight. The cells were washed thoroughly with PBS and incubated in a serum-free 10% CCK-8 medium for 2 h. Finally, the absorbance was monitored at 450 nm using a microplate reader. The results are expressed as the percentage of cell viability after different treatments compared to the group with no treatment. 4T1 cells were cultured in a glass-bottom dish,

followed by incubation with TCPH in a fresh medium for 24 h (containing 10 μg/mL TTT), and various treatments. The cells were incubated in 1 ml of serum-free medium containing 5 μM DCFH-DA for 30 min at 37 ˚C. The cells were then irradiated at 660 nm (0.3 W/cm^2) for 10 min, followed by incubation at 37 ˚C for another 30 min before CLSM imaging (emission filter: 500–550 nm; excitation wavelength: 488 nm). 4T1 cells were cultured in a glass-bottom dish, followed by treatment with TCPH in a fresh medium (containing 10 μg/mL TTT). The cells were incubated for 24 h, and further exposed to 660 nm laser (0.3 W/cm^2) irradiation for 10 min. The cells were then incubated at 37 ˚C for another 4 h, followed by staining with PI (60 μg/mL) and CA (100 μg/mL) in PBS for 10 min prior to CLSM imaging (emission filter: 550–650 nm for PI and 500–550 nm for CA; excitation wavelength: 534 nm for PI and 488 nm for CA). TCPH or TTT solution (containing 1 μg TTT) was added to 1 mL of the 4T1 cell incubation medium. After incubation for 1, 3, and 6 h, and washing with PBS, the cells were further co-stained with different bioprobes. The cells were washed with PBS and imaged using CLSM (emission filter: 650–730 nm for TCPH and TTT, and 410–500 nm for DAPI; excitation wavelength: 535 nm for TCPH and TTT, and 405 nm for DAPI). Lysosomes and mitochondria were tracked using LTG and MitoTracker Green, respectively (emission filter: 500–550 nm; excitation wavelength: 488 nm).

***In vivo* biodistribution analysis using FLI/PAI/PTI.** When tumor volume reached ~100 mm^3, mice were administered 10 μL of TCPH solution by intratumoral injection. At predetermined time points (0, 1, 6, 24, 48, 72, and 96 h), in vivo images were captured. Furthermore, in vivo PAI was also performed using an opt-acoustic tomography system at designated time intervals after the administration of TCPH. To evaluate the tissue distribution of TCPH, the corresponding tumors and major organs (heart, liver, spleen, lungs, and kidneys) were collected for ex vivo FLI, 96 h post-injection. The optimal excitation wavelength and emission filter for FLI of TCPH were 535 and 700 nm, respectively. For in vivo PTI, the infrared thermal images of mice were acquired using an E6 IR camera during irradiation at 660 nm (0.3 W/cm^2) for 5 min, 24 h after TCPH administration.

***In vivo* synergistic antitumor therapy.** When tumor volume reached ~100 mm^3, mice were randomly divided into five groups (n = 5), and the following treatments were implemented by intratumoral injection: (i) PBS (ii) TTT (iii) TCPH (iv) TTT + L and (v) TCPH + L. Laser irradiation at 660 nm (0.3 W/cm^2) was applied to the tumor sites for 10 min. The body weight and tumor volume of the treated mice were measured every two days. The tumor volume was calculated using the following formula: volume = $width^2 \times (length/2)$.

Statistical analysis. Data analyses were performed using the GraphPad Prism 9.0 software. The significance between two groups was calculated using Student's t-test ($*P<0.05$, $**P<0.01$, $***P<0.001$, $****P<0.0001$).

AUTHOR INFORMATION

Corresponding Author

Dong Wang - Center for AIE Research, Shenzhen Key Laboratory of Polymer Science and Technology, Guangdong Research Center for Interfacial Engineering of Functional Materials, College of Materials Science and Engineering, Shenzhen University, Shenzhen 518060, China; E-mail: wangd@szu.edu.cn

Ben Zhong Tang - School of Science and Engineering, The Chinese University of Hong Kong, Shenzhen (CUHK-Shenzhen), Guangdong, 518172, P.R. China; E-mail: tangbenz@cuhk.edu.cn

Hui Tan - Center for Child Care and Mental Health (CCCMH), Shenzhen Children's Hospital, Shenzhen 518034, China; E-mail: huitan@email.szu.edu.cn

Authors

Yuanwei Wang - Center for Child Care and Mental Health (CCCMH), Shenzhen Children's Hospital, Shenzhen 518034, China; Center for AIE Research, Shenzhen Key Laboratory of

Polymer Science and Technology, Guangdong Research Center for Interfacial Engineering of Functional Materials, College of Materials Science and Engineering, Shenzhen University, Shenzhen 518060, China

Penghang Chen - Institute of Lung Health and Immunity (LHI) and Comprehensive, Pneumology Center (CPC), Helmholtz Munich, Member of the German Center for Lung Research (DZL), 85764 Neuherberg, Germany; Light Innovation Technology Ltd., Shenzhen 518110, China

Haifei Wen - School of Science and Engineering, The Chinese University of Hong Kong, Shenzhen (CUHK-Shenzhen), Guangdong, 518172, P.R. China

Yixiong Gui - Center for AIE Research, Shenzhen Key Laboratory of Polymer Science and Technology, Guangdong Research Center for Interfacial Engineering of Functional Materials, College of Materials Science and Engineering, Shenzhen University, Shenzhen 518060, China

Dingyuan Yan - Center for AIE Research, Shenzhen Key Laboratory of Polymer Science and Technology, Guangdong Research Center for Interfacial Engineering of Functional Materials, College of Materials Science and Engineering, Shenzhen University, Shenzhen 518060, China

Di Huang - Light Innovation Technology Ltd., Shenzhen 518110, China

Author Contributions

The manuscript was written through contributions of all authors. All authors have given approval to the final version of the manuscript. ‡Y.W. and ‡P.C. contributed equally to this work. Y.W., P.C., H.T., D.W., and B.T. conceived the project. Y.W. and P.C. constructed the NPs, performed *in vitro* and *in vivo* experiments. H.W. and Y.G. synthesized and analyzed the molecules; D.H. completed the pulmonary hyalinization and handled the LiSM images. Y.W. wrote the manuscript. D.Y., P.C. and D.W. critically discussed the results and reviewed the manuscript; All authors discussed the results and commented on the manuscript.

Funding Sources

This work was supported by the Natural Science Foundation of China (22205095), the Science Technology Innovation Commission of Shenzhen Municipality (JCYJ20220530155415035, JCYJ20220818102804009, KQTD20210811090142053, JCYJ20220818103007014) and the Shenzhen Key Laboratory of Functional Aggregate Materials (ZDSYS20211021111400001).

Notes

The authors declare no competing financial interest.

ACKNOWLEDGEMENTS

We thank the AIE Institute (www.aietech.org.cn) for providing some AIE materials and technical assistance. The authors also acknowledge the Instrumental Analysis Center of Shenzhen University for testing services.

ASSOCIATED CONTENT

Supporting Information Available

Additional experimental section; PL spectra; The molecular docking models; ROS generation performance; Photothermal conversion behavior; Quantification analysis of comet assay; The colocalization and Z-stack CLSM images; Immunofluorescence and H&E staining images; The hemolytic effect analysis; The tumor growth curve, body weight curve and digital photos of each mouse; The LiSM images of lungs (PDF)

REFERENCES

(1) Mellman, I.; Coukos, G.; Dranoff, G. Cancer immunotherapy comes of age. *Nature* **2011,** *480*, 480-489.

(2) Murciano-Goroff, Y. R.; Warner, A. B.; Wolchok, J. D. The future of cancer immunotherapy: microenvironment-targeting combinations. *Cell Res.* **2020,** *30*, 507-519.

(3) Larkin, J.; Chiarion-Sileni, V.; Gonzalez, R.; Grob, J.-J.; Rutkowski, P.; Lao, C. D.; Cowey, C. L.; Schadendorf, D.; Wagstaff, J.; Dummer, R.; Ferrucci, P. F.; Smylie, M.; Hogg,

D.; Hill, A.; Márquez-Rodas, I.; Haanen, J.; Guidoboni, M.; Maio, M.; Schöffski, P.; Carlino, M. S.; Lebbé, C.; McArthur, G.; Ascierto, P. A.; Daniels, G. A.; Long, G. V.; Bastholt, L.; Rizzo, J. I.; Balogh, A.; Moshyk, A.; Hodi, F. S.; Wolchok, J. D. Five-Year Survival with Combined Nivolumab and Ipilimumab in Advanced Melanoma. *N. Engl. J. Med.* 2019, *381*, 1535-1546.

(4) Jiang, P.; Gu, S.; Pan, D.; Fu, J.; Sahu, A.; Hu, X.; Li, Z.; Traugh, N.; Bu, X.; Li, B.; Liu, J.; Freeman, G. J.; Brown, M. A.; Wucherpfennig, K. W.; Liu, X. S. Signatures of T cell dysfunction and exclusion predict cancer immunotherapy response. *Nat. Med.* 2018, *24*, 1550-1558.

(5) Havel, J. J.; Chowell, D.; Chan, T. A. The evolving landscape of biomarkers for checkpoint inhibitor immunotherapy. *Nat. Rev. Cancer* 2019, *19*, 133-150.

(6) Paré, L.; Pascual, T.; Seguí, E.; Teixidó, C.; Gonzalez-Cao, M.; Galván, P.; Rodríguez, A.; González, B.; Cuatrecasas, M.; Pineda, E.; Torné, A.; Crespo, G.; Martin-Algarra, S.; Pérez-Ruiz, E.; Reig, Ò.; Viladot, M.; Font, C.; Adamo, B.; Vidal, M.; Gaba, L.; Muñoz, M.; Victoria, I.; Ruiz, G.; Viñolas, N.; Mellado, B.; Maurel, J.; Garcia-Corbacho, J.; Molina-Vila, M. Á.; Juan, M.; Llovet, J. M.; Reguart, N.; Arance, A.; Prat, A. Association

between PD1 mRNA and response to anti-PD1 monotherapy across multiple cancer types. *Ann. Oncol.* **2018,** *29*, 2121-2128.

(7) Xu, Y.; Chen, C.; Guo, Y.; Hu, S.; Sun, Z. Effect of CRISPR/Cas9-Edited PD-1/PD-L1 on Tumor Immunity and Immunotherapy. *Front. Immunol.* **2022,** *13*.

(8) Rupp, L. J.; Schumann, K.; Roybal, K. T.; Gate, R. E.; Ye, C. J.; Lim, W. A.; Marson, A. CRISPR/Cas9-mediated PD-1 disruption enhances anti-tumor efficacy of human chimeric antigen receptor T cells. *Sci. Rep.* **2017,** *7*, 737.

(9) Zhang, X.; Wang, C.; Wang, J.; Hu, Q.; Langworthy, B.; Ye, Y.; Sun, W.; Lin, J.; Wang, T.; Fine, J.; Cheng, H.; Dotti, G.; Huang, P.; Gu, Z. PD-1 Blockade Cellular Vesicles for Cancer Immunotherapy. *Adv. Mater.* **2018,** *30*, 1707112.

(10) Hodi, F. S.; O'Day, S. J.; McDermott, D. F.; Weber, R. W.; Sosman, J. A.; Haanen, J. B.; Gonzalez, R.; Robert, C.; Schadendorf, D.; Hassel, J. C.; Akerley, W.; van den Eertwegh, A. J. M.; Lutzky, J.; Lorigan, P.; Vaubel, J. M.; Linette, G. P.; Hogg, D.; Ottensmeier, C. H.; Lebbé, C.; Peschel, C.; Quirt, I.; Clark, J. I.; Wolchok, J. D.; Weber, J. S.; Tian, J.; Yellin, M. J.; Nichol, G. M.; Hoos, A.; Urba, W. J. Improved Survival with Ipilimumab in Patients with Metastatic Melanoma. *N. Engl. J. Med.* **2010,** *363*, 711-723.

(11) Topalian, S. L.; Hodi, F. S.; Brahmer, J. R.; Gettinger, S. N.; Smith, D. C.; McDermott, D. F.; Powderly, J. D.; Carvajal, R. D.; Sosman, J. A.; Atkins, M. B.; Leming, P. D.; Spigel, D. R.; Antonia, S. J.; Horn, L.; Drake, C. G.; Pardoll, D. M.; Chen, L.; Sharfman, W. H.; Anders, R. A.; Taube, J. M.; McMiller, T. L.; Xu, H.; Korman, A. J.; Jure-Kunkel, M.; Agrawal, S.; McDonald, D.; Kollia, G. D.; Gupta, A.; Wigginton, J. M.; Sznol, M. Safety, Activity, and Immune Correlates of Anti–PD-1 Antibody in Cancer. *N. Engl. J. Med.* **2012,** *366*, 2443-2454.

(12) Martins, F.; Sofiya, L.; Sykiotis, G. P.; Lamine, F.; Maillard, M.; Fraga, M.; Shabafrouz, K.; Ribi, C.; Cairoli, A.; Guex-Crosier, Y.; Kuntzer, T.; Michielin, O.; Peters, S.; Coukos, G.; Spertini, F.; Thompson, J. A.; Obeid, M. Adverse effects of immune-checkpoint inhibitors: epidemiology, management and surveillance. *Nat. Rev. Clin. Oncol.* **2019,** *16*, 563-580.

(13) Naidoo, J.; Page, D. B.; Li, B. T.; Connell, L. C.; Schindler, K.; Lacouture, M. E.; Postow, M. A.; Wolchok, J. D. Toxicities of the anti-PD-1 and anti-PD-L1 immune checkpoint antibodies. *Ann. Oncol.* **2016,** *27*, 1362.

(14) McLeod, H. L.; Mariam, A.; Schveder, K. A.; Rotroff, D. M. Assessment of Adverse Events and Their Ability to Discriminate Response to Anti-PD-1/PD-L1 Antibody Immunotherapy. *J. Clin. Oncol.* **2020,** *38*, 103-104.

(15) Hsu, Patrick D.; Lander, Eric S.; Zhang, F. Development and Applications of CRISPR-Cas9 for Genome Engineering. *Cell* **2014,** *157*, 1262-1278.

(16) Doudna, J. A.; Charpentier, E. The new frontier of genome engineering with CRISPR-Cas9. *Science* **2014,** *346*, 1258096.

(17) Ran, F. A.; Hsu, P. D.; Wright, J.; Agarwala, V.; Scott, D. A.; Zhang, F. Genome engineering using the CRISPR-Cas9 system. *Nat. Protoc.* **2013,** *8*, 2281-2308.

(18) Stadtmauer, E. A.; Fraietta, J. A.; Davis, M. M.; Cohen, A. D.; Weber, K. L.; Lancaster, E.; Mangan, P. A.; Kulikovskaya, I.; Gupta, M.; Chen, F.; Tian, L.; Gonzalez, V. E.; Xu, J.; Jung, I.-y.; Melenhorst, J. J.; Plesa, G.; Shea, J.; Matlawski, T.; Cervini, A.; Gaymon, A. L.; Desjardins, S.; Lamontagne, A.; Salas-Mckee, J.; Fesnak, A.; Siegel, D. L.; Levine, B. L.; Jadlowsky, J. K.; Young, R. M.; Chew, A.; Hwang, W.-T.; Hexner, E. O.; Carreno, B. M.; Nobles, C. L.; Bushman, F. D.; Parker, K. R.; Qi, Y.; Satpathy, A. T.; Chang, H. Y.; Zhao, Y.; Lacey, S. F.; June, C. H. CRISPR-engineered T cells in patients with refractory cancer. *Science* **2020,** *367*, eaba7365.

(19) Manguso, R. T.; Pope, H. W.; Zimmer, M. D.; Brown, F. D.; Yates, K. B.; Miller, B. C.; Collins, N. B.; Bi, K.; LaFleur, M. W.; Juneja, V. R.; Weiss, S. A.; Lo, J.; Fisher, D. E.; Miao, D.; Van Allen, E.; Root, D. E.; Sharpe, A. H.; Doench, J. G.; Haining, W. N. In vivo CRISPR screening identifies Ptpn2 as a cancer immunotherapy target. *Nature* **2017,** *547*, 413-418.

(20) Zhao, L.; Luo, Y.; Huang, Q.; Cao, Z.; Yang, X. Photo-Enhanced CRISPR/Cas9 System Enables Robust PD-L1 Gene Disruption in Cancer Cells and Cancer Stem-Like Cells for Efficient Cancer Immunotherapy. *Small* **2020,** *16*, 2004879.

(21) Robert, C.; Ribas, A.; Schachter, J.; Arance, A.; Grob, J. J.; Mortier, L.; Daud, A.; Carlino, M. S.; McNeil, C. M.; Lotem, M.; Larkin, J. M. G.; Lorigan, P.; Neyns, B.; Blank, C. U.; Petrella, T. M.; Hamid, O.; Su, S. C.; Krepler, C.; Ibrahim, N.; Long, G. V. Pembrolizumab versus ipilimumab in advanced melanoma (KEYNOTE-006): post-hoc 5-year results from an open-label, multicentre, randomised, controlled, phase 3 study. *Lancet. Oncol.* **2019,** *20*, 1239-1251.

(22) Hegde, P. S.; Chen, D. S. Top 10 Challenges in Cancer Immunotherapy. *Immunity* **2020,** *52*, 17-35.

(23) Ng, C. W.; Li, J.; Pu, K. Recent Progresses in Phototherapy-Synergized Cancer Immunotherapy. *Adv. Funct. Mater.* **2018,** *28*, 1804688.

(24) Ng, C. W.; Li, J.; Pu, K. Phototherapy-Synergized Cancer Immunotherapy: Recent Progresses in Phototherapy-Synergized Cancer Immunotherapy (Adv. Funct. Mater. 46/2018). *Adv. Funct. Mater.* **2018,** *28*, 1870327.

(25) Nguyen, V.-N.; Zhao, Z.; Tang, B. Z.; Yoon, J. Organic photosensitizers for antimicrobial phototherapy. *Chem. Soc. Rev.* **2022,** *51*, 3324-3340.

(26) Xie, Z.; Fan, T.; An, J.; Choi, W.; Duo, Y.; Ge, Y.; Zhang, B.; Nie, G.; Xie, N.; Zheng, T.; Chen, Y.; Zhang, H.; Kim, J. S. Emerging combination strategies with phototherapy in cancer nanomedicine. *Chem. Soc. Rev.* **2020,** *49*, 8065-8087.

(27) Feng, B.; Zhou, F.; Hou, B.; Wang, D.; Wang, T.; Fu, Y.; Ma, Y.; Yu, H.; Li, Y. Binary Cooperative Prodrug Nanoparticles Improve Immunotherapy by Synergistically Modulating Immune Tumor Microenvironment. *Adv. Mater.* **2018,** *30*, e1803001.

(28) Deng, H.; Zhou, Z.; Yang, W.; Lin, L. S.; Wang, S.; Niu, G.; Song, J.; Chen, X. Endoplasmic Reticulum Targeting to Amplify Immunogenic Cell Death for Cancer Immunotherapy. *Nano Lett.* **2020,** *20*, 1928-1933.

(29) Wang, J.; Meng, J.; Ran, W.; Lee, R. J.; Teng, L.; Zhang, P.; Li, Y. Hepatocellular Carcinoma Growth Retardation and PD-1 Blockade Therapy Potentiation with Synthetic High-density Lipoprotein. *Nano Lett.* **2019,** *19*, 5266-5276.

(30) Zhou, F.; Feng, B.; Yu, H.; Wang, D.; Wang, T.; Ma, Y.; Wang, S.; Li, Y. Tumor Microenvironment-Activatable Prodrug Vesicles for Nanoenabled Cancer Chemoimmunotherapy Combining Immunogenic Cell Death Induction and CD47 Blockade. *Adv. Mater.* **2019,** *31*, e1805888.

(31) Pan, J.; Wang, Y.; Zhang, C.; Wang, X.; Wang, H.; Wang, J.; Yuan, Y.; Wang, X.; Zhang, X.; Yu, C.; Sun, S.-K.; Yan, X.-P. Antigen-Directed Fabrication of a Multifunctional Nanovaccine with Ultrahigh Antigen Loading Efficiency for Tumor Photothermal-Immunotherapy. *Adv. Mater.* **2018,** *30*, 1704408.

(32) Luo, J.; Xie, Z.; Lam, J. W. Y.; Cheng, L.; Chen, H.; Qiu, C.; Kwok, H. S.; Zhan, X.; Liu, Y.; Zhu, D.; Tang, B. Z. Aggregation-induced emission of 1-methyl-1,2,3,4,5-pentaphenylsilole. *Chem. Commun.* **2001,** 1740-1741.

(33) Mei, J.; Leung, N. L. C.; Kwok, R. T. K.; Lam, J. W. Y.; Tang, B. Z. Aggregation-Induced Emission: Together We Shine, United We Soar! *Chem. Rev.* **2015,** *115*, 11718-11940.

(34) Wang, S.; Hu, F.; Pan, Y.; Ng, L. G.; Liu, B. Bright AIEgen–Protein Hybrid Nanocomposite for Deep and High-Resolution In Vivo Two-Photon Brain Imaging. *Adv. Funct. Mater.* **2019,** *29*, 1902717.

(35) Qin, W.; Ding, D.; Liu, J.; Yuan, W. Z.; Hu, Y.; Liu, B.; Tang, B. Z. Biocompatible Nanoparticles with Aggregation-Induced Emission Characteristics as Far-Red/Near-Infrared Fluorescent Bioprobes for In Vitro and In Vivo Imaging Applications. *Adv. Funct. Mater.* **2012,** *22*, 771-779.

(36) Leung, N. L. C.; Xie, N.; Yuan, W.; Liu, Y.; Wu, Q.; Peng, Q.; Miao, Q.; Lam, J. W. Y.; Tang, B. Z. Restriction of Intramolecular Motions: The General Mechanism behind Aggregation-Induced Emission. *Chem.–Eur. J.* **2014,** *20*, 15349-15353.

(37) Pérez-Herrero, E.; Fernández-Medarde, A. Advanced targeted therapies in cancer: Drug nanocarriers, the future of chemotherapy. *Eur. J. Pharm. Biopharm.* **2015,** *93,* 52-79.

(38) Lv, J.; Chang, H.; Wang, Y.; Wang, M.; Xiao, J.; Zhang, Q.; Cheng, Y. Fluorination on polyethylenimine allows efficient 2D and 3D cell culture gene delivery. *J. Mater. Chem. B* **2015,** *3*, 642-650.

(39) Boussif, O.; Lezoualc'h, F.; Zanta, M. A.; Mergny, M. D.; Scherman, D.; Demeneix, B.; Behr, J. P. A versatile vector for gene and oligonucleotide transfer into cells in culture and in vivo: polyethylenimine. *Proc. Natl. Acad. Sci.* **1995,** *92*, 7297-7301.

(40) Dosio, F.; Arpicco, S.; Stella, B.; Fattal, E. Hyaluronic acid for anticancer drug and nucleic acid delivery. *Adv. Drug Delivery Rev.* **2016,** *97,* 204-236.

(41) Mattheolabakis, G.; Milane, L.; Singh, A.; Amiji, M. M. Hyaluronic acid targeting of CD44 for cancer therapy: from receptor biology to nanomedicine. *J. Drug Target.* **2015,** *23*, 605-618.

(42) Huang, L.; Li, Y.; Du, Y.; Zhang, Y.; Wang, X.; Ding, Y.; Yang, X.; Meng, F.; Tu, J.; Luo, L.; Sun, C. Mild photothermal therapy potentiates anti-PD-L1 treatment for immunologically cold tumors via an all-in-one and all-in-control strategy. *Nat. Commun.* **2019,** *10*, 4871.

(43) Galon, J.; Bruni, D. Approaches to treat immune hot, altered and cold tumours with combination immunotherapies. *Nat. Rev. Drug Discov.* **2019,** *18*, 197-218.

(44) Zhang, J.; Huang, D.; Saw, P. E.; Song, E. Turning cold tumors hot: from molecular mechanisms to clinical applications. *Trends Immunol.* **2022,** *43*, 523-545.

(45) Jiang, Y.; Upputuri, P. K.; Xie, C.; Zeng, Z.; Sharma, A.; Zhen, X.; Li, J.; Huang, J.; Pramanik, M.; Pu, K. Metabolizable Semiconducting Polymer Nanoparticles for Second Near-Infrared Photoacoustic Imaging. *Adv. Mater.* **2019,** *31*, e1808166.

(46) Jiang, Y.; Zhao, X.; Huang, J.; Li, J.; Upputuri, P. K.; Sun, H.; Han, X.; Pramanik, M.; Miao, Y.; Duan, H.; Pu, K.; Zhang, R. Transformable hybrid semiconducting polymer nanozyme for second near-infrared photothermal ferrotherapy. *Nat. Commun.* **2020,** *11*, 1857.

(47) Wen, H.; Zhang, Z.; Kang, M.; Li, H.; Xu, W.; Guo, H.; Li, Y.; Tan, Y.; Wen, Z.; Wu, Q.; Huang, J.; Xi, L.; Li, K.; Wang, L.; Wang, D.; Tang, B. Z. One-for-all phototheranostics: Single component AIE dots as multi-modality theranostic agent for fluorescence-photoacoustic imaging-guided synergistic cancer therapy. *Biomaterials* **2021,** *274,* 120892.

Table of Contents

Light Up CRISPR: Imaging-guided Gene-editing for Comprehensive Cancer Theranostics

Yuanwei Wang,[a,b]‡ Penghang Chen,[c,d]‡ Haifei Wen,[e] Yixiong Gui,[b] Dingyuan Yan,[b] Di Huang,[d] Dong Wang,[b] Ben Zhong Tang,[e]* and Hui Tan[a]**

A CRISPR-Cas9/PD-L1 system and AIEgen are combined to construct a multifunctional nanoplatform for comprehensive cancer theranostics. The generated ROS and hyperthermia do not only achieve primary tumor elimination but also regulate the tumor immune microenvironment. Genomic disruption of PD-L1 conspicuously augments its therapeutic efficacy, especially in tumor metastasis and recurrence. Exceptional multimodal imaging navigation has also been developed.